



The top-down crystallisation of Mercury's core

A.L. Edgington^{a,*}, L. Vočadlo^a, L. Stixrude^{a,b}, I.G. Wood^a, D.P. Dobson^a, E. Holmström^c

^a Department of Earth Sciences, University College London, Gower Street, WC14 6BT, UK

^b Department of Earth, Planetary, and Space Sciences, University of California, Los Angeles, CA 90095-1567, United States of America

^c Natural Resources Institute Finland (Luke), Production systems / Forest technology and logistics, Maarintie 6, 02150 Espoo, Finland

ARTICLE INFO

Article history:

Received 15 June 2017

Received in revised form 19 August 2019

Accepted 9 September 2019

Available online xxx

Editor: B. Buffett

Keywords:

planetary science

Mercury

core evolution

planetary interiors

top-down crystallization

iron alloys

ABSTRACT

The regime governing the growth of Mercury's core is unknown, but the dynamics of core growth are vital to understanding the origin and properties of the planet's weak magnetic field. Here, we use advanced first-principles methods, which include a magnetic entropy contribution, to investigate the magnetic and thermo-elastic properties of liquid Fe-S-Si and of pure liquid iron at the conditions of Mercury's core. Our results support a 'top-down' evolution of the core, whereby solid iron-rich material crystallises at shallow depths and sinks. This process would likely result in a compositionally driven dynamo within a stably stratified uppermost liquid layer, providing an explanation for the observed properties of the weak magnetic field of Mercury.

© 2019 Elsevier B.V. All rights reserved.

1. Introduction

The MESSENGER mission revealed two surprising features of Mercury's magnetic field: 1) it is anomalously weak compared to the field strength expected of an Earth-like dynamo process (Vilim et al., 2010) and 2) it is strongly asymmetric with respect to the equator, with the strength of the field in the northern hemisphere three times that in the southern hemisphere (Anderson et al., 2012). While the spatial scale of the field makes a dynamo origin likely, the origin of these unusual features is still unknown.

An important source of uncertainty is the distribution of buoyancy in Mercury's core: does buoyancy originate from a crystallizing inner core, as in Earth, or does crystallization occur from the top down (or in some more complex arrangement) (Chen et al., 2008)? MESSENGER gravity data are compatible with partial solidification of the core (Margot et al., 2012), but do not require it and cannot constrain its location (Hauck et al., 2013). Recent models of Mercury's magnetic field show that the location of the crystallizing layer is crucial: models with a crystallizing inner core do not explain the asymmetry of the field (Cao et al., 2014), and a crystallizing layer at the top may be important for weakening of the field due to magnetic shielding (Christensen, 2006). Recent work on the electrical and thermal properties of liquid Fe suggest a thermally

stratified layer at the top of Mercury's core (Silber et al., 2018), however, the effect of light alloying elements is unknown.

Here, we use ab initio simulations of the material properties of Fe alloys to constrain the crystallization regime of Mercury's core. The key material property is the adiabatic gradient $(dT/dP)_S$. If this exceeds the slope of the liquidus, crystallization proceeds from the top down, whereas if the slope of the liquidus is greater, crystallization proceeds from the bottom up, as in the Earth (Williams, 2009). The adiabatic gradient of Fe-S-Si alloys that likely compose Mercury's core is unknown, and even those of simpler systems, such as Fe-S, are highly uncertain. Here we determine the adiabatic gradient of Fe and Fe-S-Si liquid, providing important new constraints on the core dynamics of the innermost planet.

2. Methods

Our ab initio molecular dynamics simulations are based on density functional theory (Kresse and Hafner, 1993; Kresse and Hafner, 1994; Kresse and Furthmüller, 1996a, 1996b). We have chosen the system Fe₈₀S₁₀Si₁₀ (atomic %) as representative of the reducing conditions characteristic of Mercury (Nittler et al., 2011), and we also examine the pure Fe system for comparison.

The Fe-S-Si composition used in this work, Fe₈₀S₁₀Si₁₀, lies in the miscible region of the phase diagram above approximately 6 GPa (Morard and Katsura, 2010) as found throughout the core pressure range of Mercury (core-mantle boundary of Mercury is approximately 5.5 GPa (Hauck et al., 2013)) and is consistent with

* Corresponding author.

E-mail address: a.edgington.12@ucl.ac.uk (A.L. Edgington).

Chabot et al. (2014) whose models of the core composition of Mercury suggest a range of possible S and Si relative abundances that are consistent with the surface measurements of sulphur and low surface abundance of iron.

We compute the adiabatic gradient as

$$\left(\frac{dT}{dP}\right)_S = \frac{\gamma T}{K_S} \quad (1)$$

where the Grüneisen parameter, γ , and bulk modulus, K_S , are determined from accurate fits to densely spaced simulation results across a pressure-temperature regime relevant to Mercury's core and beyond (see supplementary information).

To calculate the adiabatic gradient of pure liquid iron and liquid $\text{Fe}_{80}\text{S}_{10}\text{Si}_{10}$ we performed first-principles molecular dynamics (FPMD) calculations combined with the perturbative approach to thermodynamic integration. The FPMD calculations were performed using the Vienna Ab Initio Simulation Package (VASP) (Kresse and Hafner, 1993, 1994; Kresse and Furthmüller, 1996a, 1996b); we used the generalised gradient approximation with the PW91 enhancement factor (Perdew et al., 1992, 1993) to the solution of Density Functional Theory. We used super-cell sizes of 125 atoms (Fe) and 150 atoms ($\text{Fe}_{80}\text{S}_{10}\text{Si}_{10}$, 120 iron, 15 silicon and 15 sulphur with the site occupancies chosen at random), initiated in a simple cubic structure, and projector augmented wave pseudopotentials (Blöchl, 1994; Kresse and Joubert, 1999) were used to describe the core electrons. A single k -point located at $(1/4, 1/4, 1/4)$ (Baldereschi, 1973) was used to sample the Brillouin zone, as this was found to better produce converged values of energy and pressure than simple gamma-point sampling of the Brillouin zone. We imposed a cut-off energy of 400 eV on the plane wave basis used to expand the electronic orbitals, giving total energies converged to within 5 meV/atom.

The Helmholtz free energy of the liquid is given by;

$$F(V, T, f) = E(V, T, f) - T(S_{\text{el}}(V, T, f) + S_{\text{vib}}(V, T, f) + S_{\text{conf}}(V, T, f) + S_{\text{mag}}(V, T, f)) \quad (2)$$

where E , is the internal energy, V is the volume, f is the mean magnitude of the atomic moment, and T is the temperature, which is multiplied by a sum of the electronic, vibrational, configurational and magnetic entropies (S_{el} , S_{vib} , S_{conf} and S_{mag}), where the magnetic entropy is equal to

$$S_{\text{mag}}(V, T, f) = k_B \sum \ln(\mu_i + 1) \quad (3)$$

in which μ_i is the magnitude of the local atomic moment and k_B is the Boltzmann constant. The magnetic entropy is critical to calculating the properties of a magnetic system as it acts negatively on the Helmholtz free energy and therefore may stabilise larger atomic magnetic moments to higher pressures. Hence this term impacts the behaviour of the material and affects the thermoelastic properties of magnetic liquid iron and $\text{Fe}_{80}\text{S}_{10}\text{Si}_{10}$.

We conducted first principles molecular dynamics (FPMD) calculations within the canonical NVT ensemble at a series of volumes at 2000, 3000 and 4000 K for both pure liquid iron and liquid $\text{Fe}_{80}\text{S}_{10}\text{Si}_{10}$ and at two magnetic configurations each, one with no atomic magnetic moment (the reference state) and another with the iron atomic magnetic moment constrained to be equal to $+3\mu_B$ /atom (in the $\text{Fe}_{80}\text{S}_{10}\text{Si}_{10}$ calculations the atomic magnetic moments of the silicon and sulphur atoms were equal to zero). At each temperature (2000, 3000 and 4000 K), the total pressures and volumes of both magnetic configurations were fitted to a third order Eulerian finite strain expression, the Birch-Murnaghan 3rd order equation of state, using the EoSFit code (Angel et al., 2014; see Fig. M1 in supplementary material).

In addition, we conducted spin-polarised FPMD simulations with unconstrained moments, which produced, at each volume-temperature condition, results with magnetic moments intermediate to those of our constrained moment calculations. We used these free-moment results to construct four further constant atomic magnetic moment equations of state at each temperature following the method of Holmström and Stixrude (2015).

From the equations of state, the Helmholtz free energy of each state was calculated using the following equation;

$$F(V, T, f) = F(V, T, 0) + \Delta F(V, T, f) - TS_{\text{mag}}(V, T, f) \quad (4)$$

In which F is the Helmholtz free energy, and ΔF indicates the difference in free energy given by the thermodynamic integration, i.e., ΔF includes everything except the magnetic entropy. The change in Helmholtz free energy between the lowest and higher atomic magnetic moments was calculated using the Kirkwood coupling scheme (Kirkwood, 1935) and thermodynamic integration following the method described in Holmström and Stixrude (2015).

The total Helmholtz free energy (Eq. (4)) was then used to calculate the Gibbs free energy, G , for each of the magnetic states;

$$G(P, T, f) = F(V, T, f) + VP(V, T, f) \quad (5)$$

The Gibbs free energies, $G = G(f)$, of the five magnetic states were fitted to a parabola, and the equilibrium mean magnetic moment was found by minimizing this parabolic fit with respect to f (the atomic magnetic moment; see Fig. M2 in supplementary material). This was repeated for a series of pressures and temperatures for both materials, thus giving the magnetic behaviour of pure liquid iron and liquid $\text{Fe}_{80}\text{S}_{10}\text{Si}_{10}$ at 2000, 3000 and 4000 K up to 160 GPa and ~ 60 GPa respectively.

At a series of pressures (1 GPa intervals between the lowest and highest calculated values) the volumes corresponding to each spin state were collated to find a relationship between volume and magnetic moment. From the magnetic moment relationship with pressure described above, the magnitude of the magnetic moment could be found for each pressure and thus the corresponding volume found. The isothermal volume-pressure values were then fitted to a Eulerian finite strain expression (Poirier, 2000) (Birch-Murnaghan 3rd order equations of state) the analytical derivative with respect to pressure of which determined the bulk modulus (Ita and Stixrude, 1992).

The remaining properties required to calculate the adiabatic gradient are the Grüneisen parameter and the thermal expansivity (Results; Fig. 3). To find the mean thermal expansivity between 2000 and 4000 K, the volumes at constant pressure across two temperatures (at 2000 and 4000 K) were used in the following expression;

$$\alpha = \left(\frac{\ln[V(T')/V(T)]}{T' - T} \right)_P \quad (6)$$

in which V , T and P have their usual meaning and $T' > T$ where T' and T are the two temperatures at which the volumes have been calculated (2000 and 4000 K in this work).

The final property required to calculate the adiabatic gradient was the Grüneisen parameter which can be determined using the following relationship between pressure, P , and internal energy, E ;

$$\gamma = V \left(\frac{dP}{dE} \right)_V \quad (7)$$

Thus, to calculate the Grüneisen parameter required the pressure and internal energy at constant volume. At each volume, consistent across all calculated magnetic states (volumes ranged between

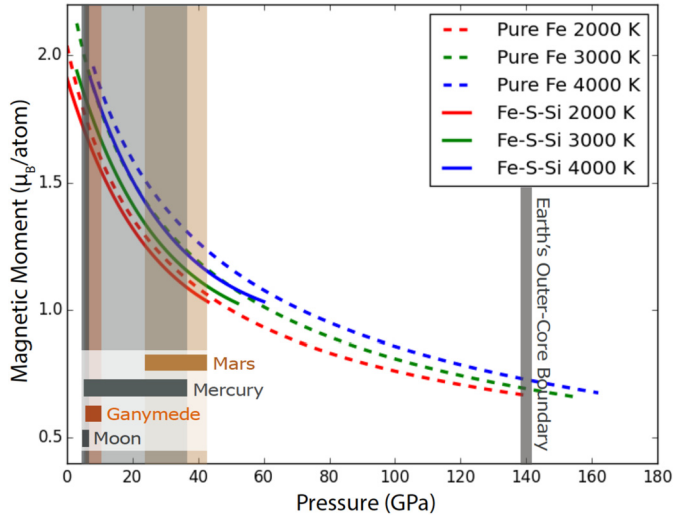


Fig. 1. The local magnetic moments of pure liquid iron (dashed lines) and liquid $\text{Fe}_{80}\text{S}_{10}\text{Si}_{10}$ (solid lines). The pressure range of Mercury's core is from Hauck et al., 2013; Ganymede's core pressure range is from Rückriemen et al., 2015; pressure range of the Moon and Mars' core are from Antonangeli et al., 2015. (For interpretation of the colours in the figure(s), the reader is referred to the web version of this article.)

13.544–10.835 \AA^3 for Fe and 14.142–11.314 \AA^3 for Fe-S-Si, see Table 2 in supplementary material), the internal energy of three simulated magnetic moment magnitudes (the highest, lowest and an intermediate spin state) were used to find a relationship between internal energy and magnetic moment. Using the fitted isothermal Birch-Murnaghan 3rd-order equations of state, the corresponding pressure could be calculated for each volume, and thus from the magnetic relationship with pressure, the predicted magnetic moment magnitude. From the pressure and internal energies at 2000 and 4000 K, the mean Grüneisen parameter between 2000–4000 K was calculated for both pure liquid iron and liquid $\text{Fe}_{80}\text{S}_{10}\text{Si}_{10}$.

3. Results

We have found that local magnetic moments of the iron atoms are large over the entire pressure-temperature range relevant to Mercury's core (Fig. 1). While they are not aligned, local magnetic moments are important because they influence physical properties including the adiabatic gradient. For example, the magnitude of the moment is known to influence the density, providing a driving force for the pressure-induced high-spin to low-spin transition seen in many materials. The local magnetic moments associated with the iron atoms decrease gradually throughout the core pressure range of Mercury and other small rocky bodies in the solar system. We find finite local magnetic moments in pure liquid iron up to at least 160 GPa, pressures at which liquid iron has been traditionally assumed to possess no local magnetic moments. A finite proportion of non-zero local magnetic moments are stabilized at high pressure and temperature by the magnetic entropy term (Eq. (4)).

Our calculated magnetic moments appear to be consistent with experiment, if we account for considerable experimental uncertainty. Whereas we find a value of $2.0\mu_B$ at 2000 K and ambient pressure, two different experimental studies yield 1.2 and $1.9\mu_B$, respectively (Weber et al., 1978; Waseda and Suzuki, 1970). At conditions where experimental measurements are more secure (measurements of bcc iron at ambient conditions), the same exchange-correlation functional that we use finds perfect agreement with experiment (Stixrude et al., 1994). Moreover, we find that the magnetic moment is slightly smaller in the alloy, consistent with trends found in Fe-Si alloys (Ishida et al., 2007).

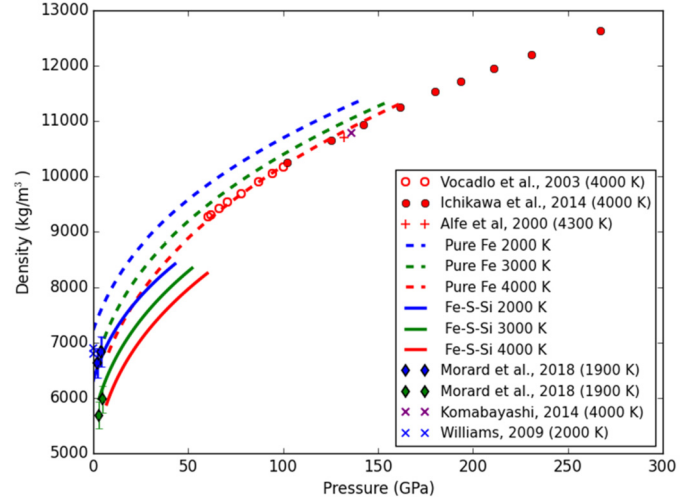


Fig. 2. The calculated densities of pure liquid iron (dashed lines) and liquid $\text{Fe}_{80}\text{S}_{10}\text{Si}_{10}$ (solid lines). Also shown are the calculated liquid iron densities at 4000 K of Vočadlo et al. (2003) and Ichikawa et al. (2014) (circles and filled circles respectively). The pure iron results of Alfè et al. (2000), Williams (2009) and Komabayashi (2014) and the Fe-S results of Morard et al. (2018) of two different compositions are also shown $\text{Fe}_{90}\text{S}_{10}$ at% (blue diamonds) and $\text{Fe}_{70.6}\text{S}_{29.4}$ at% (green diamonds).

Table 1

The fitted-parameters of the Birch-Murnaghan 3rd-order equation of state for pure liquid iron and Fe-S-Si (80:10:10 at%).

	T (K)	V_0 ($\text{\AA}^3/\text{atom}$)	K_0 (GPa)	K'
Fe	2000	12.97	55.31	8.41
	3000	14.51	38.66	7.54
	4000	15.63	36.31	6.25
Fe-S-Si	2000	13.33	50.43	8.13
	3000	15.09	33.71	7.05
	4000	17.37	17.08	7.95

Using the simulated magnetic moments of pure liquid iron and liquid Fe-S-Si, the pressure-volume relationship at 2000, 3000 and 4000 K were calculated and fitted to Eulerian finite strain expression (Birch Murnaghan 3rd order equations of state; (Poirier, 2000), Fig. 2; Table 1).

The results calculated in this work using thermodynamic integration at 4000 K are consistent with the results of Vočadlo et al. (2003), Ichikawa et al. (2014) and Alfè et al., 2000, as well as the thermodynamic model prediction of Komabayashi (2014) (Fig. 2). However, ambient densities of liquid iron at 2000 K range from 6800–6900 kg/m^3 (Williams, 2009 and references therein), which is lower than the calculated values shown here. The difference in density is of similar magnitude to the error in density of bcc iron calculated by Stixrude et al. (1994) (the PBE functional was found to overestimate the density by $\sim 3\%$) which suggests a similar overestimation has been found here. Our computed thermal expansivity is consistent with previous theory (Vočadlo et al., 2003; Ichikawa et al., 2014), Hugoniot data (Duffy and Ahrens, 1993), and with the range of proposed values at 1 bar (Williams, 2009) (Fig. 3). We find that the Grüneisen parameter increases on compression, as has been found in other studies of liquids (Vočadlo et al., 2003; Stixrude and Karki, 2005).

The adiabatic gradient of $\text{Fe}_{80}\text{S}_{10}\text{Si}_{10}$ is much greater than the slope of the liquidus, indicating top-down crystallization (Fig. 4). It is thought that the core of Mercury cannot be composed of pure iron because the melting point is too high to permit a liquid core as required by geodetic data. For comparison, we note that while the adiabatic gradient of pure iron is similar to that of our iron alloy, the slope of the pure iron liquidus is much greater, producing a more complex crystallisation scenario in a hypothetical pure

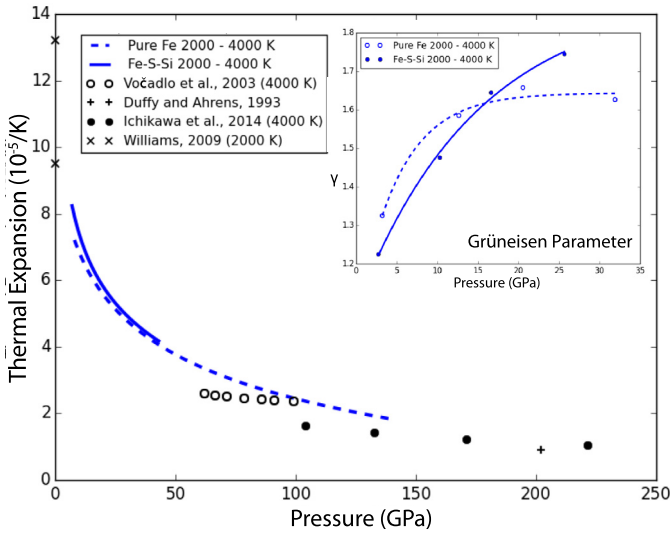


Fig. 3. The mean thermal expansion of pure liquid iron (dashed line) and $\text{Fe}_{80}\text{S}_{10}\text{Si}_{10}$ (solid line) between 2000 and 4000 K. With increasing pressure, the thermal expansivity of both materials decrease. Shown for comparison are the results of Vočadlo et al. (2003) and Ichikawa et al. (2014) (circles and filled circles respectively) who performed ab initio calculations on thermal expansion of pure liquid iron at higher temperatures, the ambient range of thermal expansivities from Williams (2009) (\times), and the Hugoniot constrain of Duffy and Ahrens (1993) (+). The inset shows our calculated Grüneisen parameter as a function of pressure.

iron core. The calculated adiabatic gradient of pure iron agrees well with the work of Williams (2009) as shown in Fig. 4, in which an estimate for the uncertainties in the pressure dependent bulk modulus and thermal expansivity used in Williams (2009) are also shown.

4. Discussion

Our results support the ‘top-down’ crystallization scenario: upon cooling, the adiabat first crosses the solidus at or near the core-mantle boundary. Iron ‘snow’ forms at the top of the core and, due to gravity, sinks to greater depths (Fig. 5). This results in the enrichment of the remaining liquid in silicon and sulphur, which is buoyantly upwelled as the iron-rich solid sinks. This process

may explain the presence of Mercury’s magnetic field, as chemical buoyancy associated with the iron ‘snow’ regime may drive a dynamo deep within the planet (Christensen, 2006). The rate of cooling at the top of the core decreases due to the latent heat of crystallisation, resulting in a sub-adiabatic and stratified upper boundary with both stable thermal and chemical gradients. At greater depths, the solid sinks into the super-liquidus region and re-melts, locally increasing the melting temperature and enriching the deep liquid core in iron. As the planet continues to cool, the temperature of the innermost region of Mercury’s core (depleted in Si and S relative to the bulk composition) falls below the liquidus of this iron-enriched composition, such that a solid inner core will begin to grow outwards from the centre of the planet. The crystallising ‘snow’ regions continue to extend deeper into the planet, eventually reaching the inner-core boundary. A ‘top-down’ crystallisation of the planet’s core has also been suggested by Dumberry and Rivoldini (2015) to best fit the geodetic observations of the planet; this is also the regime proposed to be governing the crystallisation of the cores of Ganymede (Hauck et al., 2006) and Mars (Stewart et al., 2007).

The top-down snowing state derived from our simulations may explain the weakness and asymmetry of Mercury’s field. Field generated deep within the core must diffuse through the conducting stratified layer at the top of the core, reducing the measured field strength (Hauck et al., 2013) and filtering out high-degree components of the field. Stable thermal stratification at the top of the core, and the sub-adiabatic gradient that it entails, is consistent with estimates of heat flow modelling at Mercury’s core-mantle boundary (Dumberry and Rivoldini, 2015) and with MESSENGER observations of librations and gravity field (Margot et al., 2007). Iron snow produces a volumetrically distributed source of buoyancy that can explain the observed asymmetry of the field (Cao et al., 2014). An iron snow layer at the top Mercury’s core may have laterally variable thickness, possibly contributing to the asymmetry of the field (Tian et al., 2015). Variable thickness might arise from lateral variations in heat flow at the core-mantle boundary due to mantle convection, heterogeneous distribution of heat producing elements, or the after-effects of ancient giant impacts. Upcoming missions will provide further constraints on core size, the thickness of crystallizing layers and the nature of the magnetic field (Benkhoff et al., 2010).

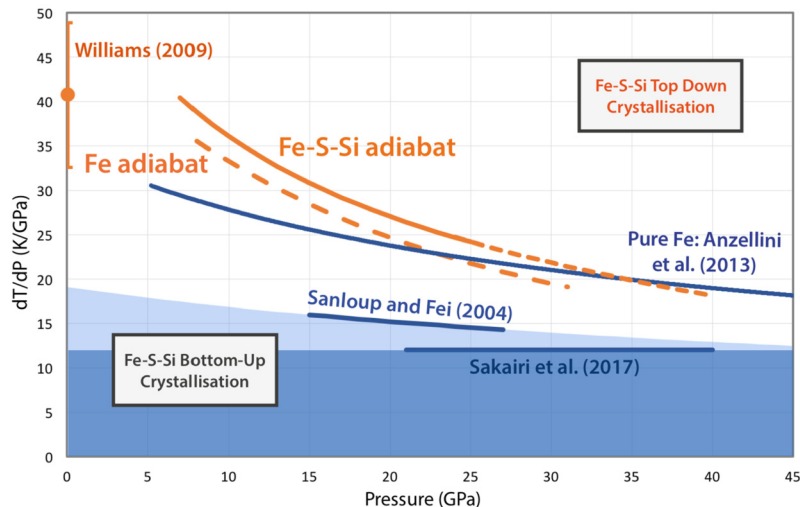


Fig. 4. The adiabatic gradient of liquid Fe-S-Si (solid orange line, small dashed orange line is an extrapolation of the calculated results) and pure liquid iron (wide dashed orange line). The blue shading is the region in which the adiabatic gradient must fall to produce bottom up crystallization and is bounded by experimental estimates of the melting slope in: Fe-18.5 wt% S-8 wt% Si (Sanloup and Fei, 2004, we fit the published data to a Simon-Glatzel equation with a 0 GPa melting temperature equal to 1800 K and differentiated to find the slope) and $\text{Fe}_{80.1}\text{S}_{12.7}\text{Si}_{7.2}$ (Sakairi et al., 2017, we fit the published curve to a straight line to obtain the slope). Also is shown the melting slope of iron (Anzellini, 2013, obtained by differentiating the analytical expression provided by the authors) and estimates of the adiabatic gradient of liquid iron at one bar (orange symbol with error bar) (Williams, 2009).

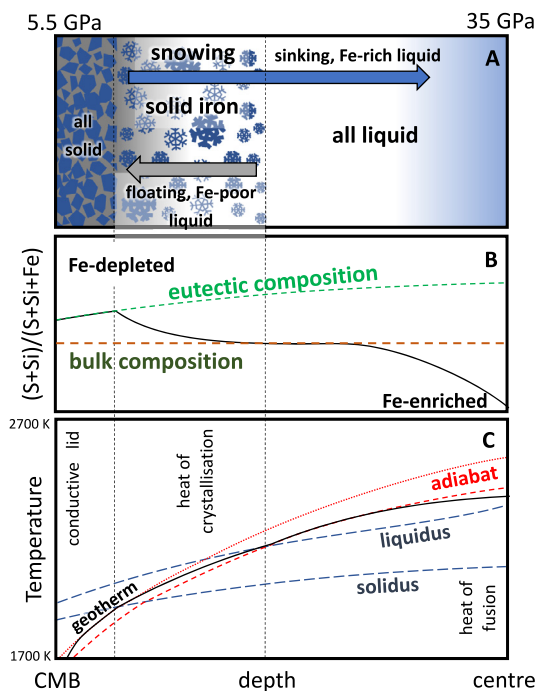


Fig. 5. Schematic describing the evolution of a hypothetical Fe-S-Si core in the planet Mercury and the consequences of a top-down scenario for the inner core composition, temperature, growth and dynamics. The range of pressure indicated is based on interior models of Mercury (Hauck et al., 2013). The range of temperature indicated is based on estimates of the temperature at the core-mantle boundary (Hauck et al., 2013) and integration of our adiabatic gradient for Fe-S-Si. Fig. 5A describes the dynamics and processes in the core in which the light-element-enriched material is shown in grey and iron-rich material represented in blue. Iron crystallisation causes segregation of light-element-enriched liquid to the top of the core (approaching the eutectic composition) and sinking of iron-rich solid. This iron then re-melts at depth to produce an iron-enriched deep core, as depicted in Fig. 5B. Crystallisation also releases latent heat of fusion, tilting the shallow geotherm away from the deep adiabat resulting in stable thermal as well as chemical gradients (Fig. 5C). Eventually the solidus is reached in the uppermost core and an entirely solid outermost core grows at the eutectic composition. Fig. 5B shows the composition field of the core with an iron-depleted upper region and iron enriched lower region due to crystallisation and sinking of iron. Fig. 5C depicts the temperature field of the core, with two adiabats extrapolated from the temperature at the solidus and liquidus and the modified geotherm which results from shallow freezing and deep re-melting of iron. Vertical dashed lines mark the depths where the geotherm crosses the solidus and liquidus. The deep core might eventually become sufficiently enriched in iron, for the iron-enriched liquidus to cross the geotherm, at which point a deep solid iron inner core will also start to grow. Interpolating between melting curves for pure Fe, $\text{Fe}_{74}\text{S}_{19}\text{Si}_7$ and FeSi (references Sakairi et al., 2017; Anzellini, 2013; Lord et al., 2010) we estimate that the melting curve for our composition would cross Mercury's adiabat at around 8 GPa.

Acknowledgements

This work has been supported by the Science and Technology Facilities Council through a PhD studentship. This work used the ARCHER UK National Supercomputing Service (<http://www.archer.ac.uk>). The authors also acknowledge the use of the UCL Grace High Performance Computing Facility (Grace@UCL), and associated support services, in the completion of this work. E.H. acknowledges financial support by the Emil Aaltonen foundation and the Academy of Finland through the Centres of Excellence Program (Project No. 251748). L.S. is supported by the European Research Council under Advanced Grant No. 291432 "MoltenEarth" (FP7/2007-2013).

Appendix A. Supplementary material

Supplementary material related to this article can be found online at <https://doi.org/10.1016/j.epsl.2019.115838>.

References

- Alfè, et al., 2000. Structure and dynamics of liquid iron under Earth's core conditions. *Phys. Rev. B* 61, 132.
- Anderson, B.J., et al., 2012. Low-degree structure in Mercury's planetary magnetic field. *J. Geophys. Res.* 117, E00L12.
- Angel, R.J., Gonzalez-Platas, J., Alvaro, M., 2014. EosFit7c and a Fortran module (library) for equation of state calculations. *Z. Kristallogr.* 229, 405–419.
- Antonangeli, D., et al., 2015. Toward a mineral physics reference model for the Moon's core. *Proc. Natl. Acad. Sci. USA* 112 (13), 3916–3919.
- Anzellini, S., 2013. Melting of iron at Earth's inner core boundary based on fast X-ray diffraction. *Science* 340 (6131), 464–466.
- Baldereschi, A., 1973. Mean-value point in the Brillouin zone. *Phys. Rev. B* 7, 5212–5215.
- Benkhoff, J., et al., 2010. BepiColombo – comprehensive exploration of Mercury: mission overview and science goals. *Planet. Space Sci.* 58, 2–20.
- Blöchl, P.E., 1994. Projector augmented-wave method. *Phys. Rev. B* 50, 17953–17979.
- Cao, H., et al., 2014. A dynamo explanation for Mercury's anomalous magnetic field. *Geophys. Res. Lett.* 41, 4127–4134.
- Chabot, et al., 2014. Experimental constraints on Mercury's core composition. *Earth Planet. Sci. Lett.* 390, 199–208.
- Chen, B., Li, J., Hauck, S.A., 2008. Non-ideal liquidus curve in the Fe-S system and Mercury's snowing core. *Geophys. Res. Lett.* 35, 10–14.
- Christensen, U.R., 2006. A deep dynamo generating Mercury's magnetic field. *Nature* 444, 1056–1058.
- Duffy, T.S., Ahrens, T.J., 1993. Thermal expansion of mantle and core materials at very high pressures. *Geophys. Res. Lett.* 20, 1103–1106.
- Dumberry, M., Rivoldini, A., 2015. Mercury's inner core size and core-crystallization regime. *Icarus* 248, 254–268.
- Hauck, S.A., Aurnou, J.M., Dombard, A.J., 2006. Sulphur's impact on core evolution and magnetic field generation on Ganymede. *J. Geophys. Res., Planets* 111, E09008.
- Hauck, S.A., et al., 2013. The curious case of Mercury's internal structure. *J. Geophys. Res., Planets* 118 (6), 1204–1220.
- Holmström, E., Stixrude, L., 2015. Spin crossover in ferropericlasite from first-principles molecular dynamics. *Phys. Rev. Lett.* 114, 117.
- Ichikawa, H., et al., 2014. The P-V-T equation of state and thermodynamic properties of liquid iron. *J. Geophys. Res., Solid Earth* 119, 240–252.
- Ishida, K., Ohno, S., Okada, T., 2007. Magnetic properties of liquid 3d transition metal-Si alloys. *J. Non-Cryst. Solids* 353, 3089–3093.
- Ita, J., Stixrude, L., 1992. Petrology, elasticity, and composition of the mantle transition zone. *J. Geophys. Res., Solid Earth* 97, 6849–6866.
- Kirkwood, J., 1935. Statistical mechanics of fluid mixtures. *J. Chem. Phys.* 3, 300–315.
- Komabayashi, T., 2014. Thermodynamics of melting relations in the system Fe-FeO at high pressure: implications for oxygen in the Earth's core. *J. Geophys. Res., Solid Earth* 119, 4164–4177.
- Kresse, G., Furthmüller, J., 1996a. Efficiency of ab-initio total energy calculations for metals and semiconductors using a plane-wave basis set. *Comput. Mater. Sci.* 6, 15–50.
- Kresse, G., Furthmüller, J., 1996b. Efficient iterative schemes for ab initio total-energy calculations using a plane-wave basis set. *Phys. Rev. B* 54, 11169–11186.
- Kresse, G., Hafner, J., 1993. Ab initio molecular dynamics for liquid metals. *Phys. Rev. B* 47, 558–561.
- Kresse, G., Hafner, J., 1994. Ab initio molecular-dynamics simulation of the liquid-metal-amorphous-semiconductor transition in germanium. *Phys. Rev. B* 49, 14251–14269.
- Kresse, G., Joubert, D., 1999. From ultrasoft pseudopotentials to the projector augmented wave method. *Phys. Rev. B* 59, 1758–1775.
- Lord, O.T., et al., 2010. The FeSi phase diagram to 150 GPa. *J. Geophys. Res.* 115 (B06208).
- Margot, J.L., Peale, S.J., Jurgens, R.F., Slade, M.A., Holin, I.V., 2007. Large longitude libration of Mercury reveals a molten core. *Science* 316, 710–714.
- Margot, J.L., et al., 2012. Mercury's moment of inertia from spin and gravity data. *J. Geophys. Res., Planets* 117, 1–11.
- Morard, G., Katsura, T., 2010. Pressure-temperature cartography of Fe-S-Si immiscible system. *Geochim. Cosmochim. Acta* 74, 3659–3667.
- Morard, G., et al., 2018. Liquid properties in the Fe-FeS system under moderate pressure: tool box to model small planetary cores. *Am. Mineral.* 103 (11), 1770–1779.
- Nittler, L.R., et al., 2011. The major-element composition of Mercury's surface from MESSENGER X-ray spectrometry. *Science* 333, 1847–1850.
- Perdew, J.P., et al., 1992. Atoms, molecules, solids, and surfaces: applications of the generalized gradient approximation for exchange and correlation. *Phys. Rev. B* 46, 6671–6687.
- Perdew, J.P., et al., 1993. Erratum: Atoms, molecules, solids, and surfaces: applications of the generalized gradient approximation for exchange and correlation. *Phys. Rev. B* 48, 4978.
- Poirier, J.P., 2000. Introduction to the Physics of the Earth's Interior. Cambridge University Press.
- Rückriemen, T., et al., 2015. The Fe snow regime in Ganymede's core: a deep seated dynamo below a stable snow zone. *J. Geophys. Res., Planets* 120 (6), 1095–1118.

- Sakairi, T., et al., 2017. Melting relations in the Fe-Si system at high pressure and temperature: implications for the planetary core. *Prog. Earth Planet. Sci.* 4, 10.
- Sanloup, C., Fei, Y., 2004. Closure of the FeSi liquid miscibility gap at high pressure. *Phys. Earth Planet. Inter.* 147 (1), 57–65.
- Silber, R.E., et al., 2018. Electrical resistivity of liquid Fe to 12 GPa: implications for heat flow in cores of terrestrial bodies. *Sci. Rep.* 8 (1), 10758.
- Stewart, A.J., Schmidt, M.W., van Westrenen, W., Liebske, C., 2007. Mars: a new core-crystallization regime. *Science* 316, 1323–1325.
- Stixrude, L., Karki, B., 2005. Structure and freezing of MgSiO₃ liquid in Earth's lower mantle. *Science* 310, 297–299.
- Stixrude, L., et al., 1994. Iron at high pressure: linearized-augmented-plane-wave computations in the generalized-gradient approximation. *Phys. Rev. B, Condens. Matter* 50 (9), 6442–6445.
- Tian, Z., Zuber, M.T., Stanley, S., 2015. Magnetic field modelling for Mercury using dynamo models with a stable layer and laterally variable heat flux. *Icarus* 260, 263–268.
- Vilim, R., Stanley, S., Hauck, S.A., 2010. Iron snow zones as a mechanism for generating Mercury's weak observed magnetic field. *J. Geophys. Res., Planets* 115.
- Vočadlo, L., et al., 2003. The properties of iron under core conditions from first principles calculations. *Phys. Earth Planet. Inter.* 140, 101–125.
- Waseda, Y., Suzuki, K., 1970. Atomic distribution and magnetic moment in liquid iron by neutron diffraction. *Phys. Status Solidi B* 39, 669–678.
- Weber, M., Knoll, W., Steeb, S., 1978. Magnetic small-angle scattering from molten elements iron, cobalt, and nickel. *J. Appl. Crystallogr.* 11 (5), 638–641.
- Williams, Q., 2009. Bottom-up versus top-down solidification of the cores of small solar system bodies: constraints on paradoxical cores. *Earth Planet. Sci. Lett.* 284 (3–4), 564–569.